

Tidal and Thermal Stresses Drive Seismicity along a Major Ross Ice Shelf Rift

S. D. Olinger^{1,2}, D. A. Wiens¹, B. P. Lipovsky², R. C. Aster³, A. A. Nyblade⁴,
R. A. Stephen⁵, P. D. Bromirski⁶, P. Gerstoft⁶, Z. Chen⁶

¹Department of Earth and Planetary Sciences, Washington University in St. Louis, St. Louis, MO, USA

²Department of Earth and Planetary Sciences, Harvard University, Cambridge, MA, USA

³Department of Geosciences, Colorado State University, Fort Collins, CO, USA

⁴Department of Geosciences, Penn State University, University Park, PA, USA

⁵Woods Hole Oceanographic Institution, Woods Hole, MA, USA

⁶Scripps Institution of Oceanography, University of California, San Diego, CA, USA

Key Points:

- 2515 icequakes associated with rift deformation on the Ross Ice Shelf are located using a double difference location algorithm.
- Icequake timing correlates with tidal phase on a diurnal timescale and inversely correlates with air temperature on multi-day and seasonal timescales.
- Ocean swell, infragravity waves and a significant tsunami arrival are not correlated with increased rift activity.

18 Abstract

19 Understanding deformation in ice shelves is necessary to evaluate the response of
20 ice shelves to thinning. We study microseismicity associated with ice shelf deformation
21 using 9 broadband seismographs deployed near a rift on the Ross Ice Shelf. From De-
22 cember 2014 - November 2016, we detect 5948 icequakes generated by rift deformation.
23 Locations were determined for 2515 events using a least squares grid-search and double-
24 difference algorithm. Ocean swell, infragravity waves and a significant tsunami arrival
25 do not affect seismicity. Instead, seismicity correlates with tidal phase on diurnal timescales
26 and inversely correlates with air temperature on multi-day and seasonal timescales. Spa-
27 tial variability in tidal elevation tilts the ice shelf, and seismicity is concentrated while
28 the shelf slopes downward toward the ice front. During especially cold periods, thermal
29 stress and embrittlement enhance fracture along the rift. We propose that thermal stress
30 and tidally-driven gravitational stress produce rift seismicity with peak activity in the
31 winter.

32 Plain Language Summary

33 In Antarctica, large bodies of floating ice called ice shelves help prevent ice on land
34 from sliding into the ocean. To predict how Antarctica might respond to climate change,
35 we need to understand how ice shelves interact with the environment, including the at-
36 mosphere and the ocean. The largest ice shelf, the Ross Ice Shelf, is over 500,000 km²
37 in area, making it the largest body of floating ice in the world. In this study, we deployed
38 9 seismographs, the same instruments used to study earthquakes, to monitor vibrations
39 and cracking within the Ross Ice Shelf over a two-year period. During that time, the in-
40 struments detected nearly 6000 fracture events along a 120 km long crack in the ice shelf.
41 We compared the timing of the cracking to air temperature data, ocean wave activity,
42 and tides to see whether these factors influenced the crack's behavior. We found that
43 fracture occurs most frequently just after high tide during winter, when the air is very
44 cold. We also found that fracture at the rift is not triggered by ocean waves. This work
45 demonstrates that Antarctic ice shelves are very sensitive to the environment and high-
46 lights the need to continue studying them.

47 **1 Introduction**

48 The need to understand marine ice sheet stability under various climate scenarios
 49 has fueled ongoing discourse about the nature and forcing of fracturing processes in
 50 floating ice shelves. Brittle deformation of large ice shelves is dominated by the propagation
 51 of large, through-cutting fracture-propagated rifts (Benn et al., 2007). Debate
 52 has largely focused on the relative importance and interactions of ocean wave-induced
 53 stresses (Holdsworth & Glynn, 1978; MacAyeal et al., 2008; Cathles et al., 2009; K. M. Brunt
 54 et al., 2011; Bromirski et al., 2010; Bromirski & Stephen, 2012; Bromirski et al., 2015;
 55 Banwell, 2017; Massom et al., 2018), glacial stresses (Bassis et al., 2005; Hulbe et al., 2010a;
 56 LeDoux et al., 2017), and rift-filling melange (Fricker et al., 2005; Larour et al., 2004;
 57 Rignot & MacAyeal, 1998; MacAyeal et al., 1998). Seismic observations have the ability
 58 to quantify small scale brittle deformation in the form of icequakes, and thus provide
 59 an efficient means to investigate the spatial and temporal extent of ice shelf fracture pro-
 60 cesses (Bassis et al., 2007; Heeszel et al., 2014; Hulbe et al., 2016; Lipovsky, 2018).

61 As part of two coupled projects to study the dynamics of the Ross Ice Shelf (RIS)
 62 and the solid Earth structure beneath (Bromirski et al., 2015), 9 broadband seismographs
 63 were deployed spanning both sides of a large rift located about 150 km south of the RIS
 64 front (Figure 1), denoted as WR4 (Walker et al., 2013). This deployment provides an
 65 important opportunity to investigate the role of various processes that drive ice shelf frac-
 66 ture. LeDoux et al. (2017) found that rift WR4's eastern tip currently is located adja-
 67 cent to a suture zone, a region of deformed ice that arrests rift propagation, and multi-
 68 year imagery has confirmed that WR4 is not actively propagating (Walker et al., 2013).
 69 Despite WR4's apparent inactivity, the RIS array detected numerous icequakes in the
 70 vicinity of the rift, which we use to determine whether the rift is undergoing active brit-
 71 tle deformation and to provide constraints on the forces influencing rift propagation.

72 **2 Data**

73 **2.1 Seismic Data**

74 This study uses data collected by two simultaneous collaborative seismograph de-
 75 ployments on the Ross Ice Shelf. We use 9 seismic stations deployed along two lines that
 76 intersect near 78.96°S, 179.88°W (Figure 1). These stations are a subset of the 34 seis-
 77 mic stations that were deployed across a much larger region (Figure 1). Each station con-

sisted of a Nanometrics T120 PHQ broadband seismometer buried about 1 meter into the firn recording at 200 samples per second and a Quanterra Q330 datalogger. The equipment was powered by solar panels in the austral summer and by lithium batteries in the winter. The instruments were deployed in November 2014 and the first year of data was retrieved November - December of 2015. The instruments were recovered, and the final year of data was retrieved in November - December of 2016.

84 **2.2 Weather and Environmental Data**

85 Temperature data from the Automatic Weather Station (AWS) project was used
86 to investigate whether seismicity is correlated with meteorological phenomena. The AWS
87 weather stations are deployed across Antarctica and record temperature, pressure, wind
88 speed, and humidity (Lazzara et al., 2012). Because of its proximity to the array and
89 the completeness of its records, we use data from station Gill, located at 79.823°S, 178.536°W
90 at a distance of 80 km from the center of the array.

91 **3 Methods**

92 **3.1 Detection and Location**

93 We utilized an automated short-term average/long-term average (STA/LTA) event
94 detection routine to form a catalog of any local activity recorded on stations with a high
95 signal-to-noise ratio. We detected 5948 unique events throughout both years of data af-
96 ter manually removing all detections of non-local seismicity. To generate arrival times
97 and to analyze the similarity of the detected events, we applied a cross-correlation and
98 clustering algorithm to the entire dataset. However, the events did not exhibit high cor-
99 relation values, and the clusters generated were not consistent across different stations
100 and components, indicating that, unlike many icequakes, the events are not true repeat-
101 ing events. A typical event waveform is shown in Supplementary Figure 1.

102 We initially located a subset of the largest events from 2015 using manually-picked
103 P and S wave arrival times. However, direct P and S wave arrivals were often small and
104 emergent, making it difficult to pick arrival times consistently. Because vertical compo-
105 nent Rayleigh wave arrivals were much easier to identify, we located the entire dataset
106 using Rayleigh wave arrival times. We calculated envelope functions for each event wave-
107 form on DR14, DR13, DR12, DR11, DR10, DR09, DR08, DR07, and RS04. Because these

108 icequake waveforms are dominated by surface waves, the maximum value of each envelope
 109 function corresponds to the arrival of Rayleigh waves. A STA/LTA threshold was
 110 also applied to prevent incorrect identification of arrivals. Using this process, Rayleigh
 111 arrival times were automatically generated for all 5948 events.

112 We located the events that had Rayleigh phase arrivals on more than five stations.
 113 We first used a simple grid-search algorithm that minimized the misfit between observed
 114 and predicted Rayleigh arrivals by calculating a summed squared error for each potential
 115 location in the grid and selecting the lowest error point. In order to calculate misfit,
 116 we back-propagated the arrivals and took the mean time as the origin time. Once
 117 satisfactory locations were obtained from the grid-search, we removed arrivals from stations
 118 with travel time residuals greater than 1 second for each event. Events now with less
 119 than five arrivals were removed, and the remaining events were relocated using a standard
 120 iterative least-squares inversion. From the resulting locations, those with location and
 121 origin time standard deviations greater than 2 km and 2 seconds were removed, and
 122 the remaining 2515 events were relocated using a double-difference relative location method.

123 To determine an accurate Rayleigh phase velocity for use in event relocation, grid-
 124 search locations were calculated using an initial velocity of 1.5 km/s. We then selected
 125 all events aligned with DR13, DR12, and DR10 and calculated the time difference between
 126 arrivals on DR13 and DR12, DR13 and DR10, and DR12 and DR10 to obtain estimates
 127 of Rayleigh velocity largely independent of source locations. A least-squares inversion
 128 was then used to determine the velocity that minimized the misfit between the observed
 129 and predicted arrival time differences calculated using the known distances between
 130 stations. This calculation resulted in a Rayleigh velocity of 1.55 km/s, which was then
 131 used in the grid-search, linearized inversion, and double-difference location methods.
 132 This Rayleigh wave velocity is similar to that predicted for a structure of slow velocity
 133 firn overlying ice.

134 **3.2 Comparison with Environmental and Weather Phenomena**

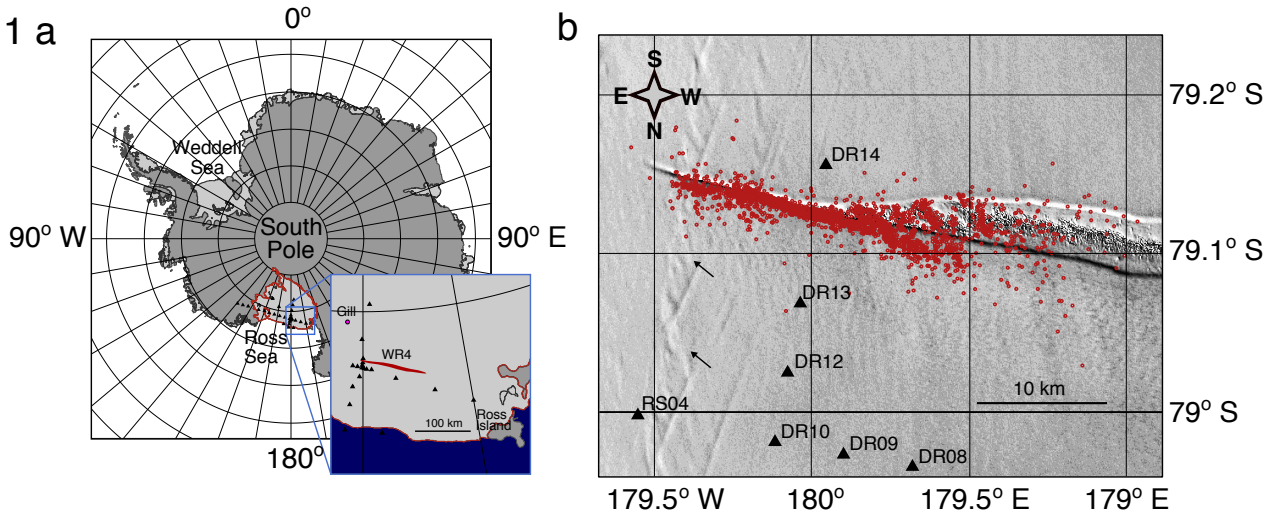
135 To investigate the relationship between rift seismicity and the atmosphere, we compare
 136 the timing of seismicity with Automatic Weather Station air temperature data from
 137 2015 and 2016 (Lazzara et al., 2012). We also compare the timing of events with tidal
 138 phase and tidal slope. Tidal heights were obtained by running the CATS2008 model, an

update to the model described by Padman, Fricker, Coleman, Howard, and Erofeeva (2002),
 for the duration of the deployment at the center of the array (DR10). To find the time
 of each high tide, local maxima were calculated for the dataset. We then calculated the
 difference in time between each event and the most recent high tide. The resulting times
 were binned by hour, yielding the number of events that occur in each hour after high
 tide. Finally, we divided by the total length of the corresponding tidal cycle to yield a
 measure of event timing binned by tidal phase. We calculated the slope at the ice shelf
 by running the CATS2008 model at both the grounding line ($82^{\circ}\text{S}, 164^{\circ}\text{E}$) and the front
 ($78.5^{\circ}\text{S}, 179^{\circ}\text{E}$), finding their difference, and dividing by the distance between the two
 points.

To investigate swell and infragravity waves, we made a spectrogram of the long pe-
 riod horizontal north-south component data from DR10. Previous work by Bromirski
 et al. (2017) found that IG waves generate greater horizontal displacements than ver-
 tical displacements on RIS, so we used the horizontal component data for our analysis
 of ocean swell and IG waves. Before generating a spectrogram, we first removed the in-
 strument response to displacement on the frequency band 0.015 Hz - 0.2 Hz. To find swell
 band power, we integrated the spectrogram over the frequency band 0.03 Hz - 0.15 Hz
 for each window used to produce the spectrogram. To find IG band power, we integrated
 the spectrogram over the frequency band 0.015 Hz - 0.03 Hz for each window used to
 produce the spectrogram. These frequency limits were selected based on the ocean wave
 classification presented in Toffoli and Bitner-Gregersen (2017).

4 Characteristics and Locations of Rift Seismicity

Icequakes with high signal-to-noise exhibit distinct P, S, surface wave, and longi-
 tudinal plate wave arrivals (Press & Ewing, 1951). Icequake events are lower frequency
 than similarly-sized tectonic earthquakes (Aki, 1967) with peak amplitudes between 1-
 4 Hz. In all cases, the icequake-associated surface waves have the largest amplitudes. We
 find that the icequakes range in size from $M_L = -2.5$ to $M_L = 0$ (Equation 1), and there
 is evidence for a b-value greater than 1 based on the statistics of larger magnitude events,
 indicating that this sequence of icequakes has a higher ratio of small to large events than
 predicted by a standard Gutenberg-Richter distribution. Typical waveforms are shown
 in Supplementary Figure 1.



160 **Figure 1. Study site and icequake locations.** (a) Locations of rift WR4, the seismograph
 161 array, and weather station Gill on the Ross Ice Shelf. Data from stations DR07 and DR06 (not
 162 shown) was additionally used to locate icequakes. (b) Locations of 2500 icequakes at WR4. East
 163 of about 180° , icequake locations fall along central axis of rift; west of 180° , icequake locations
 164 fall within en echelon features containing rift-filling melange. Arrows indicate suture zone fabric.

175 The icequake epicenters were located using a double difference method and auto-
 176 mated picks of peak Rayleigh wave arrival times on the vertical component seismogram.
 177 The icequakes are located along a 30 km segment of the rift (Figure 1), associated with
 178 three broad regional patterns of icequake activity. First, icequakes located east of about
 179 180°E are aligned with the central axis of the rift. Because the observed icequakes have
 180 high amplitude surface waves relative to body waves, it is likely that the icequakes oc-
 181 cur near the ice shelf surface (Lough et al., 2015). Possible sources include fracture along
 182 the upper edges of the rift walls and collision, settling, or fracture of the blocks of ice
 183 within the melange.

184 Second, many of the icequakes west of about 180°E occur along a series of en ech-
 185 elon features within the wider region of rift-filling melange. Because the standard de-
 186 viations of relative icequake locations are typically around 100 m and because of the strong
 187 spatial association of the events with the en echelon shear zone features, we are confi-
 188 dent that these events originated within the melange and were not incorrectly located
 189 events occurring along the rift walls. We therefore interpret this second group of icequakes
 190 to be caused by deformation of the rift-filling melange. Because events in the melange

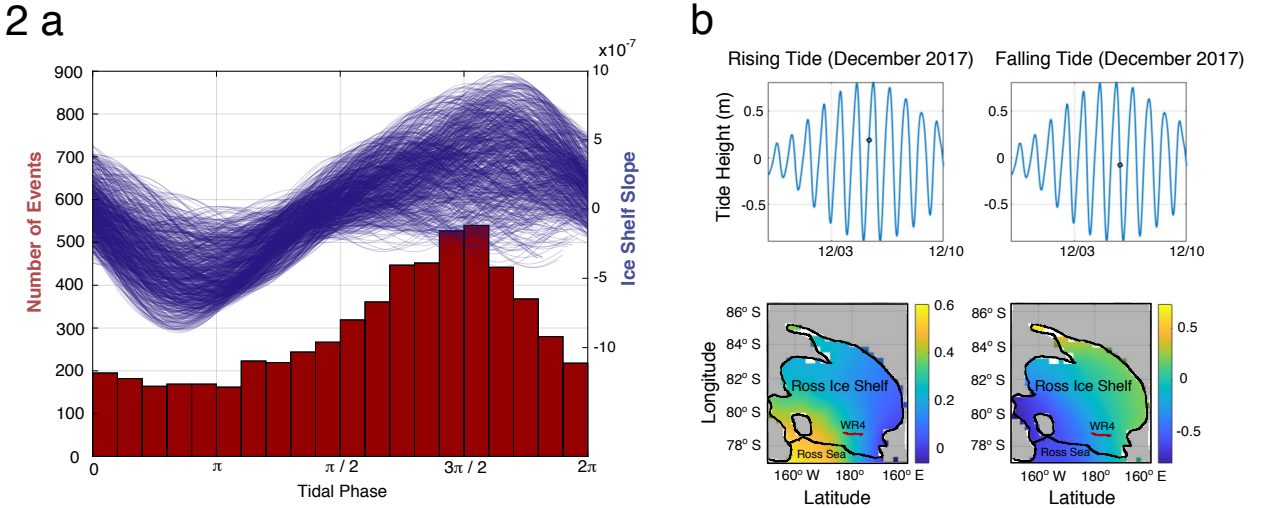
begin to occur where the rift widens, we speculate that the type of brittle ice shelf deformation recorded here may cause widening at the middle of the rift. See Supplementary Figure 2 for a more detailed view of rift morphology.

Third, events decrease in number west of about 179.5°E and distant events are typically less precisely located. To determine whether the apparent concentration of icequakes is an artifact of our network geometry, we examined the magnitude of the events at various positions along the rift. We find that the prevalence of low magnitude events decreases with distance from the intersection of the array and the rift, suggesting that the apparent decrease in seismicity away from the network may be the result of attenuation of similar-sized signals from more distant icequakes. It is therefore possible that relatively uniform levels of seismicity occur along the entire rift.

Icequakes are not clustered in front of the rift tip as was previously observed at the actively-propagating Loose Tooth Rift in the Amery Ice Shelf (Bassis et al., 2008; Heeszel et al., 2014) but instead cease abruptly where the rift reaches the adjacent suture zone at around 179.5°W. This decrease in seismicity is not due to reduced array detection capability to the west, as very small events are detected in the rift near the rift tip. We interpret the lack of icequakes at the rift tip to indicate a lack of brittle deformation in this region. Since westward propagation of the WR4 rift tip has currently stagnated (Walker et al., 2013; LeDoux et al., 2017), our inferred lack of brittle deformation is therefore consistent with rift stagnation in suture zones (Hulbe et al., 2010b; McGrath et al., 2014; Kulessa et al., 2014; Borstad et al., 2017).

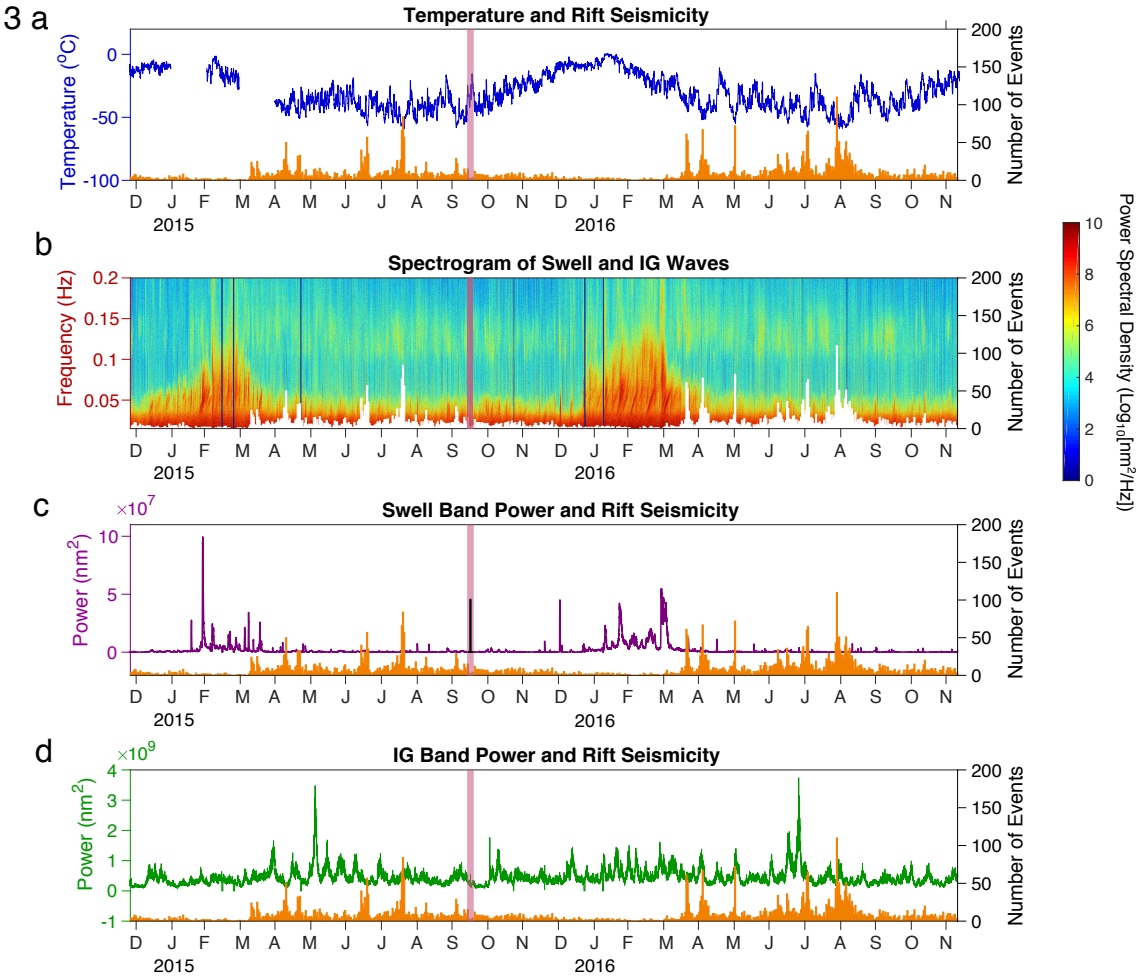
5 Ice Shelf Slope from Ocean Tides Controls Diurnal Patterns in Seismicity

We observe tidal modulation of the icequake activity (Figure 2a). As tides rise, the level of seismicity increases until about 5 hours after high tide, when the level of seismicity begins to fall. The timing of events within a day is well-correlated with the tidally-modulated slope of the ice shelf, with the highest seismicity rates when the entire Ross Ice Shelf slopes downwards toward the ocean (Figure 2b). When the shelf tilts, a horizontal component of gravitational force arises in the plane of the ice shelf. If the shelf is tilted towards the continent, the rift is under compression and we see low levels of seismicity; if the shelf is tilted seawards, the rift is subjected to additional extensional stress and we see high levels of seismicity. Using the CATS2008 tide model (Padman et al., 2002),



212 **Figure 2. Tidal slope and rift seismicity.** (a) Histogram of event timing as a function of
 213 tidal phase plotted with ocean surface slope (blue lines) for each tidal cycle during the duration
 214 of the deployment. (b) Modeled tidal heights at 81.75°S , -175°W , the center of the ice shelf
 215 (top), and in map view across the RIS (bottom) demonstrating the ocean surface slope relation-
 216 ships shown in (a). Red dots in the top figures identify the timing of the ice shelf height maps.
 217 Tidal heights were obtained using the CATS2008 tidal model (Padman et al., 2002).

229 we find that this 5-hour delay corresponds to a maximum tidally-induced tilt of the en-
 230 tire Ross Ice Shelf (Figure 2). We calculate the maximum stretching stress that could
 231 affect the rift associated with this tilt to be $\rho_i g \alpha L$ where ρ_i is the ice density, g is the
 232 acceleration due to gravity, L is the distance from the rift to the ice front, and α is the
 233 tidally-induced tilt angle. For $\alpha = 10*10^{-7}$, this suggests maximum stretching stresses
 234 on the order of 1 kPa, in agreement with stress due to sea surface tilt calculated by Bassis
 235 et al. (2008). Our findings are consistent with previous observations of tidally-modulated
 236 glacial seismicity (Barruol et al., 2013; Podolskiy et al., 2016) and tidally-modulated ice
 237 shelf flow (K. Brunt et al., 2010; Makinson et al., 2012). Furthermore, they suggest that
 238 stretching stresses from tidal cycles are preferentially released at rifts and may be as-
 239 sociated with the processes that widen rifts after formation.



240 **Figure 3. Ocean swell, infragravity waves, temperature and rift seismicity.** (a)
241 Surface temperatures from AWS station Gill (blue) plotted with the histogram of rift seismicity
242 (orange) as a function of time during the deployment. (b) Spectrogram showing swell and infra-
243 gravity wave band power. Black bars indicate data gaps. (c) Ocean swell power (purple line) in
244 the frequency band 0.03 - 0.15 Hz plotted with the histogram of rift seismicity. (d) Infragravity
245 wave power (green line) in the frequency band 0.015 - 0.03 Hz, plotted with the histogram of rift
246 seismicity. Spectral analysis used long period north-south component data from station DR10.
247 The Illapel, Chile tsunami arrival is indicated in pink on each panel of the figure. The seasonal
248 trend in seismicity corresponds to seasonal temperature variation, and wintertime swarms coin-
249 cide with periods of extreme cold and not with swell or infragravity waves.

250 6 Temperature Controls Multi-day and Seasonal Patterns in Seismic- 251 ity

252 The detected icequakes exhibit a distinct seasonality that correlates with surface
253 temperature data (Figure 3a). Temperature data was recorded by station Gill (Figure

254 1) of the Antarctic Weather Stations project (Lazzara et al., 2012), at a distance of 80
255 km from the center of the array. In the Antarctic summer (Dec/Jan/Feb), very low lev-
256 els of seismicity are observed. However, as soon as temperatures begin to decline rapidly
257 at the beginning of winter in both 2015 and 2016, the average number of events per day
258 increases dramatically, with days containing over 20 events becoming common. Further-
259 more, large and rapid decreases in temperature appear to be associated with days of par-
260 ticularly high activity. The coldest periods of 2015 and 2016 both correspond to days
261 with the largest number of icequakes. Although seismic noise levels are highest in the
262 summer, examination of the temporal pattern of the larger events shows that the sea-
263 sonal pattern of seismicity is not due to the seasonality of the seismic noise floor (Sup-
264 plementary Information and Supplementary Figure 3).

265 There are two potential mechanisms that could account for the correlation between
266 icequake activity and temperature. First, ice experiences low temperature embrittlement
267 when loaded in compression (Petrovic, 2003). It is therefore plausible that tidal stresses
268 result in ductile deformation at high temperatures but brittle icequake-related deforma-
269 tion at lower temperatures. This explanation is consistent with studies that find seasonal
270 variability of ice shelf material properties (Bromirski & Stephen, 2012).

271 Second, the uppermost portion of the ice experiences thermal contraction in response
272 to rapid temperature drops, and would thus be under tensional stress, as is observed for
273 sea ice during cold weather (Evans & Untersteiner, 1971; Richter-Menge & Elder, 1998;
274 Dempsey et al., 2018). Similar behavior has been observed in some alpine glaciers, which
275 exhibit thermal fracturing in response to cold night-time temperatures (Podolskiy et al.,
276 2018; Zhang et al., 2019). Although we have not obtained source parameters for these
277 events, the association between the icequakes and tensional tidal stress, and their loca-
278 tion in a rift zone, suggest that the events are dominantly tensional. Since both the tidal
279 and the thermal mechanisms produce horizontal tensional stress, it is likely that they
280 act in concert. Because short-period temperature fluctuations only propagate to a depth
281 of several meters in glacial ice (Giese & Hawley, 2015), shallow icequake locations are
282 consistent with the correlation between icequake activity and surface air temperatures.
283 However, we note the possibility that enhanced cold air circulation within the rift may
284 cause thermal contraction deeper in the ice than would otherwise be possible.

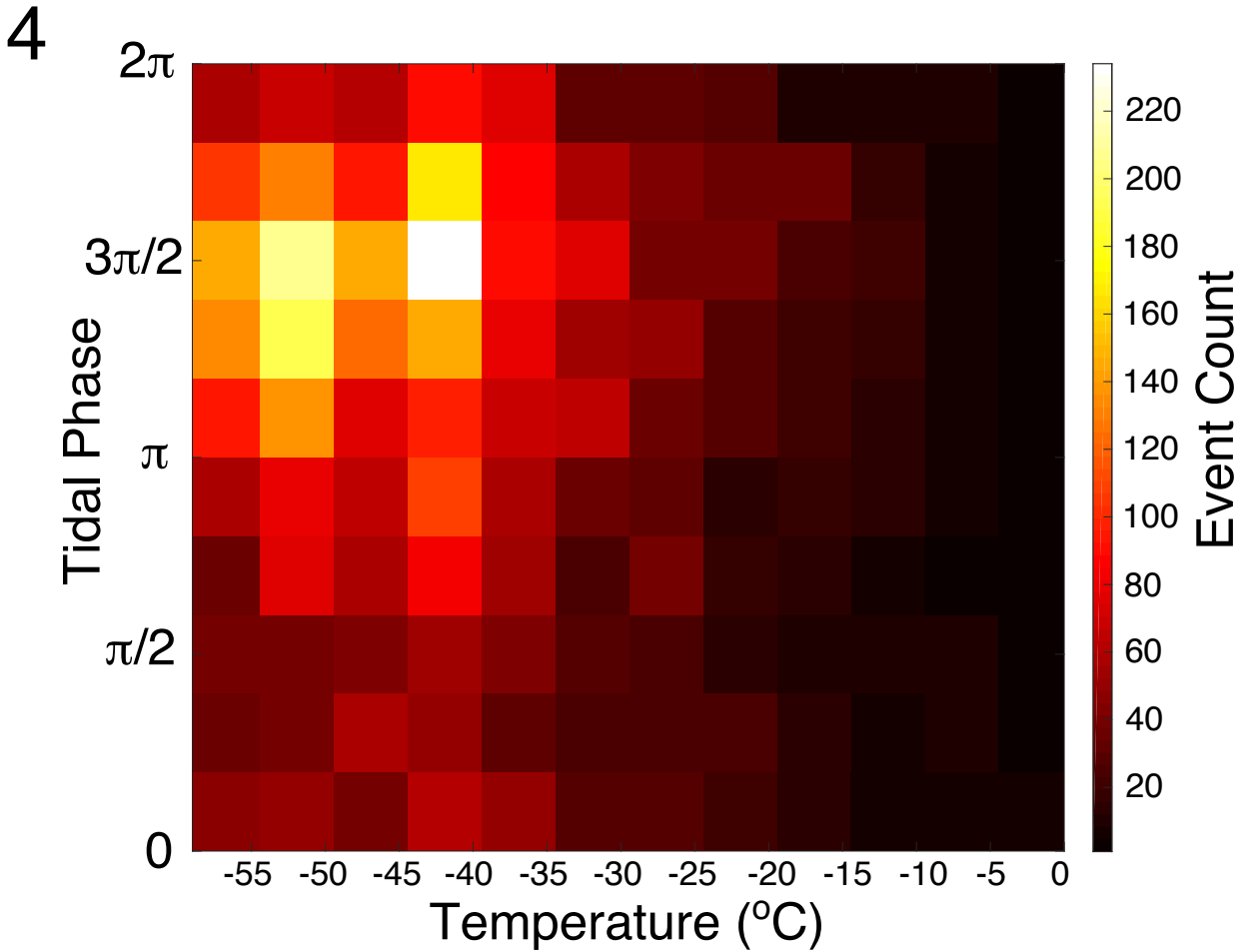
285 7 Rift Seismicity is Insensitive to Ocean Swell and Infragravity Waves

286 Both ocean swell and infragravity (IG) waves are poorly correlated with seismic-
 287 ity at WR4. We analyze the contribution of swell and IG waves by spectral analysis of
 288 the horizontal north-south component data from station DR10, since ocean waves gen-
 289 erate large horizontal displacements on RIS (Bromirski et al., 2017). Because sea ice at-
 290 tenuates ocean waves (Massom et al., 2018), swell energy only reaches the array during
 291 the austral summer, when seasonal sea ice is minimal in extent. Rift seismicity is far less
 292 frequent in the austral summer than in the winter, and periods that contain significant
 293 swell energy correspond to very low levels of seismicity at the rift (Figure 3b, 3c). Fur-
 294 thermore, when peak levels of seismicity are observed during wintertime icequake swarms,
 295 minimal power is observed in the swell band.

296 Infragravity waves are damped less effectively than swell by winter sea ice (Bromirski
 297 & Stephen, 2012), and IG wave excitation of the RIS is detected by the array year-round
 298 (Figure 3b). We find that IG band power is poorly correlated with seismicity (Figure
 299 3d). Most swarms occur on days that lack significant IG band power, and the largest IG
 300 events recorded at the array do not correspond to swarms of seismicity. Finally, the base-
 301 line level of IG power is nearly constant throughout the year and does not explain the
 302 seasonality observed in rift seismicity. On September 17, 2015, a tsunami generated by
 303 the M_w 8.3 Illapel, Chile earthquake reached the ice shelf, exciting horizontal displace-
 304 ments of about 7 cm at DR10 (Bromirski et al., 2017). The tsunami arrival is marked
 305 in Figure 3 and is particularly visible in the swell power time-series. However, the tsunami
 306 does not correspond to an increase in seismicity at WR4. This is consistent with pre-
 307 vious findings that only rifts open to the ocean at the calving front propagate when a
 308 tsunami arrives (Walker et al., 2013), further suggesting that WR4 is not subject to sig-
 309 nificant wave-induced fracture.

314 8 Conclusions

315 Two primary environmental factors control rift seismicity at WR4. Diurnally, the
 316 timing of events is well-correlated with tidally-driven changes in ice shelf slope. Over longer
 317 time periods, the timing of events is well-correlated with air temperature, with peak lev-
 318 els of activity in the winter and swarms of events on particularly cold days. The com-
 319 bination of these two factors explains the temporal patterns in seismicity that we observe



310 **Figure 4. Density plot of number of events as a function of tidal phase and tem-**
 311 **perature.** Temperature data is from weather station Gill (Figure 1). Peak levels of seismicity
 312 are observed when temperature is low and when the shelf is most highly sloped downward toward
 313 the ice front during falling tide.

320 here and demonstrates the high environmental sensitivity of rift deformation. Figure 4
 321 illustrates that maximal icequake activity occurs during cold periods when the ice shelf
 322 is sloping downward toward the ice front. We note that while low levels of icequake ac-
 323 tivity are observed at low tide, no rift seismicity is observed above -10°C . From this anal-
 324 ysis, we conclude that although thermal and tidal stresses are both important in gen-
 325 erating shallow icequake activity, temperature exerts the most significant control on brit-
 326 tle deformation at WR4.

327 The sequence of WR4 icequakes differs from patterns of seismicity seen in prop-
 328 agating rifts, and the correspondence of the locations to en echelon shear zone features
 329 suggests that fracture may occur within the melange filling the rift. Swell and IG waves
 330 were not correlated with rift seismicity, though they may still exert some influence on
 331 rift behavior at RIS and at other ice shelves. The timing of rift activity at WR4 appears
 332 to be primarily modulated by thermal and tidal stresses arising from fluctuations in air
 333 temperature and changes in ice shelf slope, and this work represents a novel demonstra-
 334 tion of tidal influence on ice shelf processes far from the grounding line. On the Ross Ice
 335 Shelf, thermal and tidal stresses act in concert with ice shelf stresses, but not wave-induced
 336 stresses, to drive brittle deformation that may widen a major rift.

337 Acknowledgments

338 NSF grants PLR-1142518, 1141916, and 1142126, supported S. D. Olinger and D.
 339 A. Wiens, R. C. Aster, and A. A. Nyblade respectively. NSF grant PLR-1246151 sup-
 340 ported P. D. Bromirski, P. Gerstoft, and Z. Chen. NSF grant OPP-1744856 and CAL-
 341 DPR-C1670002 also supported P. D. Bromirski. NSF grant PLR-1246416 supported R.
 342 A. Stephen. The Incorporated Research Institutions for Seismology (IRIS) and the PASS-
 343 CAL Instrument Center at New Mexico Tech provided seismic instruments and deploy-
 344 ment support. The RIS seismic data (network code XH) are archived at the IRIS Data
 345 Management Center, <http://ds.iris.edu/ds/nodes/dmc/>.

346 S. D. Olinger catalogued and located the icequakes, completed the analysis of seis-
 347 micity and environmental forcing, and drafted the manuscript. D. A. Wiens and B. P.
 348 Lipovsky provided significant contributions to the analysis and interpretation of results
 349 and to the manuscript text. D. A. Wiens, R. C. Aster, A. A. Nyblade, R. A. Stephen,
 350 P. Gerstoft, and P. D. Bromirski collaborated to design and obtain funding for the de-
 351 ployment. D. A. Wiens, R. C. Aster, R. A. Stephen, P. Gerstoft, P. D. Bromirski, and
 352 Z. Chen deployed and serviced seismographs in Antarctica. All authors provided val-
 353 uable feedback, comments, and edits to the manuscript text.

354 References

- 355 Aki, K. (1967). Scaling law of seismic spectrum. *Journal of Geophysi-*
 356 *cal Research (1896-1977)*, 72(4), 1217-1231. Retrieved from <https://>

- 357 agupubs.onlinelibrary.wiley.com/doi/abs/10.1029/JZ072i004p01217
358 doi: 10.1029/JZ072i004p01217
- 359 Banwell, A. (2017, 04 19). Ice-shelf stability questioned. *Nature*, 544, 306 EP -. Re-
360 trieved from <https://doi.org/10.1038/544306a>
- 361 Barruol, G., Cordier, E., Bascou, J., Fontaine, F. R., Legrésy, B., & Lescarmon-
362 tier, L. (2013). Tide-induced microseismicity in the mertz glacier ground-
363 ing area, east antarctica. *Geophysical Research Letters*, 40(20), 5412–
364 5416. Retrieved from <https://doi.org/10.1002/2013GL057814> doi:
365 doi:10.1002/2013GL057814
- 366 Bassis, J. N., Coleman, R., Fricker, H. A., & Minster, J. B. (2005). Episodic prop-
367 agation of a rift on the amery ice shelf, east antarctica. *Geophysical Research
368 Letters*, 32(6). Retrieved from <https://doi.org/10.1029/2004GL022048>
369 doi: doi:10.1029/2004GL022048
- 370 Bassis, J. N., Fricker, H. A., Coleman, R., Bock, Y., Behrens, J., Darnell, D.,
371 ... Minster, J.-B. (2007). Seismicity and deformation associated with
372 ice-shelf rift propagation. *Journal of Glaciology*, 53(183), 523–536. doi:
373 10.3189/002214307784409207
- 374 Bassis, J. N., Fricker, H. A., Coleman, R., & Minster, J.-B. (2008). An inves-
375 tigation into the forces that drive ice-shelf rift propagation on the amery
376 ice shelf, east antarctica. *Journal of Glaciology*, 54(184), 17–27. doi:
377 10.3189/002214308784409116
- 378 Benn, D. I., Warren, C. R., & Mottram, R. H. (2007). Calving processes and
379 the dynamics of calving glaciers. *Earth-Science Reviews*, 82(3), 143 - 179.
380 Retrieved from [http://www.sciencedirect.com/science/article/pii/
381 S0012825207000396](http://www.sciencedirect.com/science/article/pii/S0012825207000396) doi: <https://doi.org/10.1016/j.earscirev.2007.02.002>
- 382 Borstad, C., McGrath, D., & Pope, A. (2017). Fracture propagation and stability
383 of ice shelves governed by ice shelf heterogeneity. *Geophysical Research Letters*,
384 44(9), 4186–4194.
- 385 Bromirski, P. D., Chen, Z., Stephen, R. A., Gerstoft, P., Arcas, D., Diez, A., ...
386 Nyblade, A. (2017). Tsunami and infragravity waves impacting antarc-
387 tic ice shelves. *Journal of Geophysical Research: Oceans*, 122(7), 5786–
388 5801. Retrieved from <https://doi.org/10.1002/2017JC012913> doi:
389 doi:10.1002/2017JC012913

- 390 Bromirski, P. D., Diez, A., Gerstoft, P., Stephen, R. A., Bolmer, T., Wiens, D. A.,
 391 ... Nyblade, A. (2015). Ross ice shelf vibrations. *Geophysical Research
 Letters*, 42(18), 7589–7597. Retrieved from <https://doi.org/10.1002/2015GL065284> doi: doi:10.1002/2015GL065284
- 394 Bromirski, P. D., Sergienko, O. V., & MacAyeal, D. R. (2010). Transoceanic infra-
 395 gravity waves impacting antarctic ice shelves. *Geophysical Research Letters*,
 396 37(2). Retrieved from <https://agupubs.onlinelibrary.wiley.com/doi/abs/10.1029/2009GL041488> doi: 10.1029/2009GL041488
- 398 Bromirski, P. D., & Stephen, R. A. (2012). Response of the ross ice shelf, antarctica,
 399 to ocean gravity-wave forcing. *Annals of Glaciology*, 53(60), 163–172. doi: 10
 400 .3189/2012AoG60A058
- 401 Brunt, K., King, M., Fricker, H., & Macayeal, D. (2010, 04). Flow of the ross ice
 402 shelf, antarctica, is modulated by the ocean tide. *Journal of Glaciology*, 56,
 403 157-161. doi: 10.3189/002214310791190875
- 404 Brunt, K. M., Okal, E. A., & MacAyeal, D. R. (2011). Antarctic ice-shelf calving
 405 triggered by the honshu (japan) earthquake and tsunami, march 2011. *Journal
 406 of Glaciology*, 57(205), 785–788. doi: 10.3189/002214311798043681
- 407 Cathles, L. M., Okal, E. A., & MacAyeal, D. R. (2009). Seismic observations
 408 of sea swell on the floating ross ice shelf, antarctica. *Journal of Geo-
 409 physical Research: Earth Surface*, 114(F2). Retrieved from <https://agupubs.onlinelibrary.wiley.com/doi/abs/10.1029/2007JF000934> doi:
 410 10.1029/2007JF000934
- 412 Dempsey, J. P., Cole, D. M., & Wang, S. (2018). Tensile fracture of a single
 413 crack in first-year sea ice. *Phil. Trans. R. Soc. A*, 376(2129), 20170346.
 414 Retrieved from <https://app.dimensions.ai/details/publication/pub.1106250569andhttp://rsta.royalsocietypublishing.org/content/376/2129/20170346.full.pdf> (Exported from https://app.dimensions.ai on
 415 2019/03/14) doi: 10.1098/rsta.2017.0346
- 418 Evans, R. J., & Untersteiner, N. (1971). Thermal cracks in floating ice sheets.
 419 *Journal of Geophysical Research (1896-1977)*, 76(3), 694–703. Retrieved
 420 from <https://doi.org/10.1029/JC076i003p00694> doi: doi:10.1029/
 421 JC076i003p00694
- 422 Fricker, H. A., Young, N. W., Coleman, R., Bassis, J. N., & Minster, J. B.

- 423 (2005). Multi-year monitoring of rift propagation on the amery ice shelf,
424 east antarctica. *Geophysical Research Letters*, 32(2). Retrieved from
425 <https://doi.org/10.1029/2004GL021036> doi: doi:10.1029/2004GL021036
- 426 Giese, A. L., & Hawley, R. L. (2015). Reconstructing thermal properties of firn at
427 summit, greenland, from a temperature profile time series. *Journal of Glaciol-*
428 *ogy*, 61(227), 503–510. doi: 10.3189/2015JoG14J204
- 429 Heeszel, D. S., Fricker, H. A., Bassis, J. N., O’Neal, S., & Walter, F. (2014). Seismic-
430 ity within a propagating ice shelf rift: The relationship between icequake loca-
431 tions and ice shelf structure. *Journal of Geophysical Research: Earth Surface*,
432 119(4), 731–744. Retrieved from <https://doi.org/10.1002/2013JF002849>
433 doi: doi:10.1002/2013JF002849
- 434 Holdsworth, G., & Glynn, J. (1978, 08). Iceberg calving from floating glaciers by a
435 vibrating mechanism. *Nature*, 274, 464-466. doi: 10.1038/274464a0
- 436 Hulbe, C. L., Klinger, M., Masterson, M., Catania, G., Cruikshank, K., & Bugni, A.
437 (2016). Tidal bending and strand cracks at the kamb ice stream ground-
438 ing line, west antarctica. *Journal of Glaciology*, 62(235), 816–824. doi:
439 10.1017/jog.2016.74
- 440 Hulbe, C. L., LeDoux, C., & Cruikshank, K. (2010a). Propagation of long frac-
441 tures in the ronne ice shelf, antarctica, investigated using a numerical model
442 of fracture propagation. *Journal of Glaciology*, 56(197), 459–472. doi:
443 10.3189/002214310792447743
- 444 Hulbe, C. L., LeDoux, C., & Cruikshank, K. (2010b). Propagation of long fractures
445 in the Ronne Ice Shelf, antarctica, investigated using a numerical model of
446 fracture propagation. *Journal of Glaciology*, 56(197), 459–472.
- 447 Kulessa, B., Jansen, D., Luckman, A. J., King, E. C., & Sammonds, P. R. (2014).
448 Marine ice regulates the future stability of a large Antarctic ice shelf. *Nature*
449 *communications*, 5, 3707.
- 450 Larour, E., Rignot, E., & Aubry, D. (2004). Modelling of rift propagation on ronne
451 ice shelf, antarctica, and sensitivity to climate change. *Geophysical Research*
452 *Letters*, 31(16). Retrieved from <https://doi.org/10.1029/2004GL020077>
453 doi: doi:10.1029/2004GL020077
- 454 Lazzara, M. A., Weidner, G. A., Keller, L. M., Thom, J. E., & Cassano, J. J.
455 (2012). Antarctic automatic weather station program: 30 years of polar

- 456 observation. *Bulletin of the American Meteorological Society*, 93(10), 1519–
457 1537. Retrieved from <https://doi.org/10.1175/BAMS-D-11-00015.1> doi:
458 10.1175/BAMS-D-11-00015.1
- 459 LeDoux, C. M., Hulbe, C. L., Forbes, M. P., Scambos, T. A., & Alley, K. (2017).
460 Structural provinces of the ross ice shelf, antarctica. *Annals of Glaciology*,
461 58(75pt1), 88–98. doi: 10.1017/aog.2017.24
- 462 Lipovsky, B. (2018). Ice shelf rift propagation and the mechanics of wave-
463 induced fracture. *Journal of Geophysical Research: Oceans*, 123(6), 4014–
464 4033. Retrieved from <https://doi.org/10.1029/2017JC013664> doi:
465 doi:10.1029/2017JC013664
- 466 Lough, A. C., Barchek, C. G., Wiens, D. A., Nyblade, A., & Anandakrishnan,
467 S. (2015). A previously unreported type of seismic source in the firn layer
468 of the east antarctic ice sheet. *Journal of Geophysical Research: Earth
Surface*, 120(11), 2237–2252. Retrieved from <https://doi.org/10.1002/2015JF003658> doi: doi:10.1002/2015JF003658
- 469 MacAyeal, D. R., Okal, E. A., Aster, R. C., & Bassis, J. N. (2008). Seismic and hy-
470 droacoustic tremor generated by colliding icebergs. *Journal of Geophysical Re-
471 search: Earth Surface*, 113(F3). Retrieved from <https://doi.org/10.1029/2008JF001005> doi: doi:10.1029/2008JF001005
- 472 MacAyeal, D. R., Rignot, E., & Hulbe, C. L. (1998). Ice-shelf dynamics near the
473 front of the filchner-ronne ice shelf, antarctica, revealed by sar interferometry:
474 model/interferogram comparison. *Journal of Glaciology*, 44(147), 419–428.
475 doi: 10.3189/S0022143000002744
- 476 Makinson, K., King, M. A., Nicholls, K. W., & Gudmundsson, G. H. (2012,
477 5). Diurnal and semidiurnal tideinduced lateral movement of ronne ice
478 shelf, antarctica. *Geophysical Research Letters*, 39(10). Retrieved from
<https://doi.org/10.1029/2012GL051636> doi: 10.1029/2012GL051636
- 479 Massom, R. A., Scambos, T. A., Bennetts, L. G., Reid, P., Squire, V. A., & Stam-
480 merjohn, S. E. (2018). Antarctic ice shelf disintegration triggered by sea ice
481 loss and ocean swell. *Nature*, 558(7710), 383–389. Retrieved from <https://doi.org/10.1038/s41586-018-0212-1> doi: 10.1038/s41586-018-0212-1
- 482 McGrath, D., Steffen, K., Holland, P. R., Scambos, T., Rajaram, H., Abdalati, W.,
483 & Rignot, E. (2014). The structure and effect of suture zones in the Larsen C

- 489 Ice Shelf, Antarctica. *Journal of Geophysical Research: Earth Surface*, 119(3),
490 588–602.
- 491 Padman, L., Fricker, H. A., Coleman, R., Howard, S., & Erofeeva, L. (2002). A
492 new tide model for the antarctic ice shelves and seas. *Annals of Glaciology*, 34,
493 247–254. doi: 10.3189/172756402781817752
- 494 Petrovic, J. (2003, 01). Review mechanical properties of ice and snow. *Journal of*
495 *Materials Science*, 38, 1-6. doi: 10.1023/A:1021134128038
- 496 Podolskiy, E. A., Fujita, K., Sunako, S., Tsushima, A., & Kayastha, R. B. (2018).
497 Nocturnal thermal fracturing of a himalayan debris-covered glacier revealed
498 by ambient seismic noise. *Geophysical Research Letters*, 45(18), 9699-9709.
499 Retrieved from <https://agupubs.onlinelibrary.wiley.com/doi/abs/10.1029/2018GL079653> doi: 10.1029/2018GL079653
- 500 Podolskiy, E. A., Sugiyama, S., Funk, M., Walter, F., Genco, R., Tsutaki, S., ...
501 Ripepe, M. (2016). Tide-modulated ice flow variations drive seismicity near
502 the calving front of bowdoin glacier, greenland. *Geophysical Research Letters*,
503 43(5), 2036–2044. Retrieved from <https://doi.org/10.1002/2016GL067743>
504 doi: doi:10.1002/2016GL067743
- 505 Press, F., & Ewing, M. (1951). Propagation of elastic waves in a floating
506 ice sheet. *Eos, Transactions American Geophysical Union*, 32(5), 673–
507 678. Retrieved from <https://doi.org/10.1029/TR032i005p00673> doi:
508 doi:10.1029/TR032i005p00673
- 509 Richter-Menge, J. A., & Elder, B. C. (1998). Characteristics of pack ice stress in
510 the alaskan beaufort sea. *Journal of Geophysical Research: Oceans*, 103(C10),
511 21817–21829. Retrieved from <https://doi.org/10.1029/98JC01261> doi: doi:
512 10.1029/98JC01261
- 513 Rignot, E., & MacAyeal, D. R. (1998). Ice-shelf dynamics near the front of the
514 filchner—ronne ice shelf, antarctica, revealed by sar interferometry. *Journal of*
515 *Glaciology*, 44(147), 405–418. doi: 10.3189/S0022143000002732
- 516 Toffoli, A., & Bitner-Gregersen, E. M. (2017). Types of ocean surface waves,
517 wave classification. In *Encyclopedia of maritime and offshore engineering* (p. 1-8).
518 American Cancer Society. Retrieved from <https://onlinelibrary.wiley.com/doi/abs/10.1002/9781118476406.emoe077>
519 doi: 10.1002/9781118476406.emoe077
- 520

- 522 Walker, C., Bassis, J., Fricker, H., & Czerwinski, R. (2013). Structural and envi-
523 ronmental controls on antarctic ice shelf rift propagation inferred from satel-
524 lite monitoring. *Journal of Geophysical Research: Earth Surface*, 118(4),
525 2354–2364. Retrieved from <https://doi.org/10.1002/2013JF002742> doi:
526 doi:10.1002/2013JF002742
- 527 Zhang, T., Chen, Y., Ding, M., Shen, Z., Yang, Y., & Guan, Q. (2019). Air-
528 temperature control on diurnal variations in microseismicity at laohugou
529 glacier no. 12, qilian mountains. *Annals of Glaciology*, 112. doi: 10.1017/
530 aog.2018.34